Published in IEEE Transactions on Terahertz Science and Technology,
vol.4(4), pp.490-500, 2014

Time-Domain Numerical Modeling of THz Photoconductive Antennas

Enrique Moreno, Mario Fernández Pantoja, *Senior Member, IEEE*, Salvador G. Garcia, *Member, IEEE*, Amelia Rubio Bretones, *Senior Member, IEEE*, and Rafael Gómez Martin, *Senior Member, IEEE*

***Abstract*—This paper presents a computational procedure to simulate the time-domain behavior of photoconductive antennas made of semiconductor and metal materials. Physical modeling of semiconductor devices at terahertz regime can be achieved by applying joint electronic and electromagnetic procedures, e.g., solving a coupled system of equations inferred from Poisson's drift-diffusion and Maxwell's equations. A set of discrete equations are derived by applying a combined finite-difference methodology for the previous steady-state and the finite-difference time-domain procedure for the transient regime. The results for the radiated electric field at broadside direction show good agreement with the experimental results previously reported in the literature.**

***Index Terms*—Finite-difference time-domain (FDTD), photoconductive antennas (PACs), semiconductor device modeling, terahertz sources.**

I. Introduction

DESPITE being introduced for more than 30 years ago, the design and manufacture of efficient sources operating in the terahertz regime currently remain an active topic of research [1]–[3]. In fact, the development of sources that can provide adequate power will define the future of THz systems, which are usually limited by the loss propagation factor [4]. Today, the choice of THz sources for systems operating in THz regime is made among: 1) laser-based sources (quantum-cascade lasers and optically pumped molecular lasers), which provide maximum power but present drawbacks in terms of size, weight, and cost [2]; 2) the solid-state sources (e.g., the microvacuum traveling-wave tube) [3], as an intermediate solution with advantages in terms of mechanical properties and price but with the disadvantage of reduced power; and 3) the photonics-based sources (e.g., optical rectifiers, photomixers, and photoconductive antennas), which present serious problems in terms of delivered power yet remain unbeatable as low-profile devices [1]. In this context, this paper is intended to be a computational assessment of the radiation parameters in photoconductive antennas, as an initial step toward developing photoconductive sources able to increase the delivered power in THz systems. Photoconductive antennas (PCAs) are widely used in applications such as THz spectroscopy [5]. Their ability to produce time-domain waveforms ranging from several tenths of GHz up to 5–10 THz is appropriate for testing signatures of materials in THz regime with a single pulse [6]. The first device designed for this purpose was the Auston switch [7], which confirmed the ability of photoconductive materials to propagate and radiate transient electromagnetic waves within the range of the subpicoseconds, as previously reported [8]. Laser pulses were later used to excite photoconductive antennas and to generate terahertz pulses [5], [9], and since then experimental measurements have been made from different semiconductors (e.g., LT-GaAs [10], [11], InGaAs [12], [13] or SiC [14]), emphasizing the advantages and disadvantages of each photoconductive material. Furthermore, CAD techniques used to design innovative PCAs have also been described. A simple numerical approach was made by formulating an equivalent current injected into the gap, modeled as a function of the incident laser power, which acts as a source term in Maxwell's curl equations [9]. However, this assumption neglects the mutual coupling between the equations governing the current generation at the gap and Maxwell's equations. Other semi-analytical approaches proposed one-dimensional models of the source currents in order to derive the radiated electric field [15], [16], but the assumptions of those techniques are only accomplished for some geometries (e.g., large apertures or symmetric electrodes). Thus, full-wave numerical models were then introduced, and different implementations of finite-difference time-domain (FDTD) techniques were proposed for solving a coupled drift-diffusion model and Maxwell's equation model [17]–[22]. Further improvements to match numerical and experimental data sought a better description of the steady state [23], and a high-accuracy model developed for electron devices [24] was included for photomixers [25].

The main objective of this paper is to present computational procedures and explicit equations leading to reproduce the experimental behavior of PCAs. Eventually, this formulation will enable the exploration of CAD geometries of PCA which may outperform the performance of the actual ones. Also, procedures described in this paper incorporate all of the abovementioned numerical contributions (e.g., solution of Poisson and continuity equations or the employment of the Shockley–Read–Hall recombination model), and add the following improvements in the calculations to assess the performance of PCAs: 1) the accurate nonequilibrium distribution of carriers in the steady state; 2) the consideration of nonhomogeneous mobilities in

Manuscript received September 10, 2013; revised January 04, 2014; accepted May 15, 2014. Date of publication June 12, 2014; date of current version June 26, 2014. This work was supported in part by the Spanish Ministry of Education under Project CSD2008-00068, the Junta de Andalucia Project P09-TIC-5327, the EU FP7/2007-2013, under grant 205294 (HIRF-SE project), and the Spanish National Project TEC2010-20841-C04-04

The authors are with the Department of Electromagnetism and Matter Physics, University of Granada, 18071 Granada, Spain (e-mail: emorenop@ugr.es; mario@ugr.es; salva@ugr.es; arubio@ugr.es; rgomez@ugr.es).

Color versions of one or more of the figures in this paper are available online at http://ieeexplore.ieee.org.

Digital Object Identifier 10.1109/TTHZ.2014.2327385

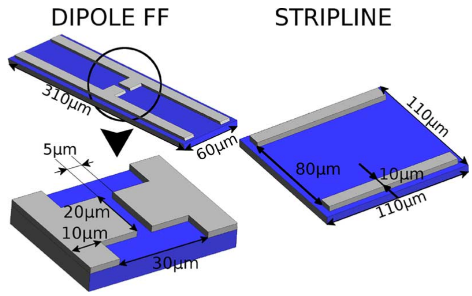

Fig. 1. Typical photoconductive antennas: the (a) face-to-face and (b) stripline dipoles. Metallic parts are depicted in light gray, semiconductor materials in blue (dark gray). Dimensions correspond to validation examples of Section IV.

the semiconductor; 3) the calculation of the divergence of electron and hole currents through Bernoulli's functions, which is required for higher numerical accuracy in nonlinear spatial distribution of carriers; 4) a stable marching-on-in-time procedure, derived through a double update of carrier distributions at each timestep considered for electric- or magnetic-field calculation; and 5) a set of standalone, explicit numerical equations which can be implemented without any external commercial software.

For this purpose, Section II describes the physical phenomena involved in the radiation of THz waves, through the drift-diffusion model coupled to a time-domain version of Maxwell's equations. Section III shows a stable computational algorithm produced by a discretization of the resulting system of partial differential equations. For the sake of brevity, some of the numerical equations have been moved to the Appendix. Finally, some results are depicted not only for the validation of the procedure but also as evidence of the potential of the method to provide physical insight in PCAs.

II. Physical Description of PCAs at THz Regime

As pointed out in the Introduction, several configurations of semiconductor and metallic materials to form the so-called photoconductive switch have been reported [5], [7], [10], [11]. For historical reasons and without loss of generality, the numerical description of PCAs presented here is based on the Auston switch configuration, in which a semiconductor is biased by external electrodes located on the top of the bulk structure in different geometries, such as the face-to-face (FF) or stripline (SL) dipoles (Fig. 1) [26]. When considering these kinds of devices of total dimensions in the micrometer range, the electromagnetic radiation phenomena at THz frequencies can be described by a set of coupled partial differential equations, which have to take into account the following physical processes: 1) the initial redistribution of carriers by a biasing DC electric-field; 2) the generation of electrons and holes (e-h) inside the semiconductor, as a consequence of an impinging laser pulse; and 3) a directive radiation of electromagnetic waves, as a result of the acceleration of these carriers generated under the biased field.

As is well known, the electromagnetic radiation is related to the dynamics of charge and current distributions [27]. However, the relevance of an accurate solution of the steady state should not be neglected because the physical description of the semiconductor depends strongly on the biasing electric field [26] [28]. Thus, the initial distribution of carriers and currents as well as the nonhomogeneous carrier mobilities in the semiconductor has to be inferred from the steady-state solution, as a step prior to calculating radiation parameters of the PCA [29].

The steady state at any point $\vec{r}$ of the semiconductor is described by the Poisson's equation for electrostatic fields, as well as by the steady formulation of the continuity equations for holes and electrons as follows:

$$\nabla\cdot(\nabla\phi(\vec{r})) = \frac{q}{\varepsilon}\left(n0(\vec{r}) - p0(\vec{r}) - C(\vec{r})\right) \quad (1)$$

$$\nabla\cdot\vec{J}_{n0}(\vec{r}) = qR0(\vec{r}) \quad (2)$$

$$\nabla\cdot\vec{J}_{p0}(\vec{r}) = -\,qR0(\vec{r}) \quad (3)$$

where $n0(\vec{r})$ and $p0(\vec{r})$ correspond to the steady-state electric-charge concentration per volume unit for electrons and holes, respectively, $\phi(\vec{r})$ accounts for the electrostatic potential, $C(\vec{r}) = N_D^+(\vec{r}) - N_A^-(\vec{r})$ is the net doping concentration distribution, signifying the balance of donor and acceptor ions, and q and ε signify the electron charge and the electric permittivity, respectively. Electrostatic field is derived as $\vec{E}_0(\vec{r}) = -\nabla\phi(\vec{r})$. In the continuity equations (2) and (3), while $\vec{J}_{n0}(\vec{r})$ and $\vec{J}_{p0}(\vec{r})$ are the steady-state electric currents for electron and holes, which can be added to form the total steady-state electric current $\vec{J}_0(\vec{r})$, we have

$$\begin{aligned}\vec{J}_0(\vec{r}) &= \vec{J}_{n0}(\vec{r}) + \vec{J}_{p0}(\vec{r})\\ &= q(\mu_n(\vec{r})\,n0(\vec{r}) + \mu_p(\vec{r})\,p0(\vec{r}))\vec{E}_0(\vec{r})\\ &\quad + qV_T\left(\mu_n(\vec{r})\nabla n0(\vec{r}) - \mu_p(\vec{r})\nabla p0(\vec{r})\right)\end{aligned} \quad (4)$$

and $R0(\vec{r})$ is the recombination rate of carriers in the semiconductor at steady-state, which can be expressed by the SRH model [30] including Auger recombination [31]

$$\begin{aligned}R0(\vec{r}) = &\left(n0(\vec{r})\,p0(\vec{r}) - n_i^2\right)\left(C_{An}n0(\vec{r}) + C_{Ap}p0(\vec{r})\right)\\ &+ \frac{n0(\vec{r})\,p0(\vec{r}) - n_i^2}{\tau_n\left(p_1 + p0(\vec{r})\right) + \tau_p\left(n_1 + n0(\vec{r})\right)}\end{aligned} \quad (5)$$

where τ_n and τ_p are the electron and hole lifetime, C_{An} and C_{Ap} are the Auger recombination coefficients for electron and hole concentrations, n_i accounts for the intrinsic concentration of carriers, and n_1 and p_1 are auxiliary quantities defined as the electrons and holes concentrations, respectively, which would exist if the Fermi energy level was at the trap energy level.

Transient electromagnetic fields $\vec{E}(\vec{r},t)$ and $\vec{H}(\vec{r},t)$ are described by classical Maxwell equations

$$\varepsilon\partial_t\vec{E}(\vec{r},t) = \nabla\wedge\vec{H}(\vec{r},t) - \vec{J}(\vec{r},t) \quad (6)$$

$$\mu\partial_t\vec{H}(\vec{r},t) = -\,\nabla\wedge\vec{E}(\vec{r},t) \quad (7)$$

where μ is the magnetic permeability, and $\vec{J}(\vec{r},t)$ is the total current in the semiconductor. In contrast to the usual electromagnetic devices, electromagnetic fields in the semiconductor-based PCAs are produced by adding electron and hole currents $\vec{J}(\vec{r},t) = \vec{J}_n(\vec{r},t) + \vec{J}_p(\vec{r},t)$, which are predicted by the drift-diffusion model in the form

$$\begin{aligned}\vec{J}_n(\vec{r},t) = &\,q\mu_n(\vec{r})\left(n(\vec{r},t) + n0(\vec{r})\right)\left(\vec{E}(\vec{r},t) + \vec{E}_0(\vec{r})\right)\\ &+ q\mu_n(\vec{r})V_T\nabla\left(n(\vec{r},t) + n0(\vec{r})\right)\end{aligned} \quad (8)$$

$$\vec{J}_p(\vec{r},t) = q\mu_p(\vec{r})(p(\vec{r},t) + p0(\vec{r}))\left(\vec{E}(\vec{r},t) + \vec{E}_0(\vec{r})\right) - q\mu_p(\vec{r})V_T\nabla(p(\vec{r},t) + p0(\vec{r})) \quad (9)$$

where $n(\vec{r},t)$ and $p(\vec{r},t)$ correspond to the transient electric-charge concentration for electrons and holes, respectively, $\mu_n(\vec{r})$, $\mu_p(\vec{r})$ are the non-homogenous field-dependent mobilities for electrons and holes [32], respectively, and V_T is the thermal voltage of the semiconductor. It is noticeable that (8) and (9) present separately the transient and steady-state contributions of fields and densities of charges, which has been done to allow the numerical discretization explained in Section III. Also, it worth noting that, for these devices, the electrostatic field $\vec{E}_0(\vec{r})$ is much higher than transient field $\vec{E}(\vec{r},t)$, and approximations $\mu_n(\vec{r},t) \approx \mu_n(\vec{r})$ and $\mu_p(\vec{r},t) \approx \mu_p(\vec{r})$ can be applied to save computational time without a significant penalty in accuracy. Once known $\vec{E}_0(\vec{r})$, several models of field-dependent mobilities can be applied to calculate $\mu_n(\vec{r})$ [33], being the parallel-field dependent models appropriate for PCAs [28].

The joint set of PDEs required for an appropriate numerical model of PCAs in the transient stage is completed by the continuity charge equations for electrons and holes

$$\partial_t n(\vec{r},t) = -RG(\vec{r},t) + q^{-1}\nabla\cdot\vec{J}_n(\vec{r},t) \quad (10)$$
$$\partial_t p(\vec{r},t) = -RG(\vec{r},t) - q^{-1}\nabla\cdot\vec{J}_p(\vec{r},t) \quad (11)$$

where $RG(\vec{r},t) = R(\vec{r},t) - G(\vec{r},t)$ is the net rate of recombination which accounts for the generation-recombination of carriers in the semiconductor. For recombination processes at any point $(\vec{r},t)$, R is

$$R = \frac{np}{\tau_n(p_1+p) + \tau_p(n_1+n)} + np(C_{An}n + C_{Ap}p). \quad (12)$$

For the generation of carriers, function G accounts for the photoelectric phenomena by applying a Gaussian function to describe the increase rate of the (e-h) pairs [34]. Then, generation at any point $\vec{r} = (x,y,z)$ is

$$G(\vec{r},t) = W_0\eta_{QE}(z)h(x,y)f(z,t) \quad (13)$$

where $W_0 = I_0\lambda_\gamma\alpha/hc$ is the maximum generation rate, which includes the parameters α as the photonic absorption coefficient, and I_0 and λ_γ as, respectively, the optical intensity and the wavelength of the laser beam. The quantum efficiency $\eta_{QE}(z)$ is [34]

$$\eta_{QE}(z) = T\xi\left(1 - e^{-\alpha(z-z_0)}\right) \quad (14)$$

where T and ξ are, respectively, the transmittance in the vacuum-semiconductor interface and the rate of pairs (e-h) which contribute to the total electric current. Finally, the spatial distribution of carriers takes the form

$$h(x,y) = e^{-\left((x-x_0/\sigma_x)^2 + (y-y_0/\sigma_y)^2\right)} \quad (15)$$
$$f(z,t) = e^{-\left(\alpha(z-z_0) + (t-t_0-z-z_0/v_m/\sigma_t)^2\right)} \quad (16)$$

where σ_x, σ_y, and σ_t are the spatial and temporal distribution of the spot laser, (x_0, y_0, z_0) is considered the point on the surface where the center of the spot laser impinges, and v_m corresponds to the velocity of the photons in the semiconductor.

Therefore, once the steady state is solved by applying (1)–(3), (6)–(7), and (10)–(11) accurately describe the carrier distributions and electromagnetic fields in the PCAs in the transient THz regime. However, theoretical solution for practical setups is not available, and computational models can be implemented only through a discretized formulation, which will be developed in the following section.

III. Numerical Solution of PCAs at THz Regime

The numerical solution of the PDEs can be achieved by means of finite-difference techniques. However, time-domain procedures are known to have stability issues, and thus an explicit and stable formulation is not straightforward [35]. Moreover, the relevance of an accurate solution of the steady state has been shown [25], not only because of the bias field but also of the non-homogeneous spatial mobility [28]. Therefore, the steady state is solved by combining the usual difference schemes for Poisson's (1) with a local description of the density of carriers based on Bernoulli's functions, as proposed in [24] to improve the numerical models of semiconductors in electron-device simulations.

Thus, for a cuboid mesh of size $(\Delta x_i, \Delta y_j, \Delta z_k)$, where $\{\mathrm{i},\mathrm{j},\mathrm{k}\}$ corresponds to the index of the cuboid, the discretized form of Poisson's equation is given by

$$\bar{\delta}_1\bar{\phi}_1 + \bar{\delta}_2\bar{\phi}_2 + \delta_\Sigma\phi_{i,j,k} = \frac{q}{\varepsilon}(n0_{i,j,k} - p0_{i,j,k} - C_{i,j,k}) \quad (17)$$

where $\phi_{i,j,k}$, $n0_{i,j,k}$, $p0_{i,j,k}$, and $C_{i,j,k}$ are, respectively, the electrostatic potential, electron density, hole density, and net concentration charge at any discrete point of the mesh. Also, auxiliary potential $\bar{\phi}_1$, $\bar{\phi}_2$ and geometrical δ_{ij}, and δ_Σ parameters are defined in Appendix A for the sake of brevity.

As it pointed out above, a finite-difference formulation for the divergence operator in (2) and (3) results in solutions with poor accuracy. The main reason for this is the exponential change in the distributions of carriers between near neighbors in the mesh as a function of the electrostatic potential, which produce significant errors for a numerical calculation of the divergence of the electric currents when a moderate mesh size is used. Instead of reducing the mesh size, which would lead to unaffordable computational resources for PCAs of usual dimensions, we can be use the Bernoulli function $B(x) = x/e^x - 1$ to describe the local variation of the carrier distribution. In this way, (2) and (3) can be expressed as

$$V_T\sum_{w=1}^{3}\left(\bar{\beta}_{n0w}\left(\bar{n0}_w\right)^T\right) - R0 = 0 \quad (18)$$
$$V_T\sum_{w=1}^{3}\left(\bar{\beta}_{p0w}\left(\bar{p0}_w\right)^T\right) - R0 = 0 \quad (19)$$

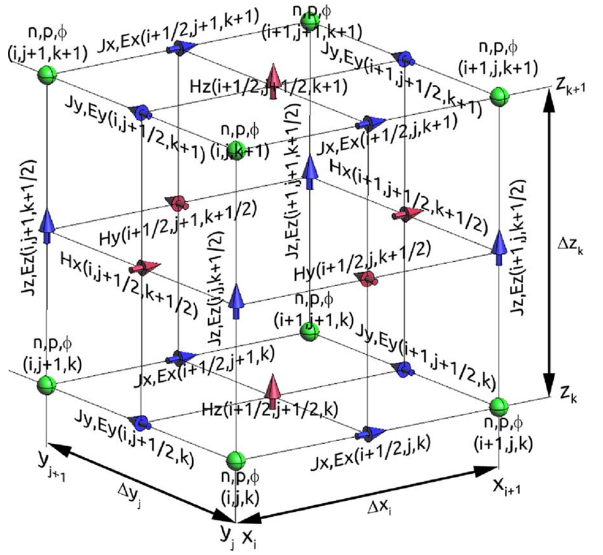

Fig. 2. Extended Yee's cell to include carrier distributions.

where auxiliary functions $\bar{\beta}_{n0}$, $\bar{\beta}_{p0}$, $\bar{n}0$, and $\bar{p}0$ are detailed in Appendix A. Discrete recombination values $R0_{i,j,k}$ are calculated by a substitution of $n0_{i,j,k}$ and $p0_{i,j,k}$ in (12).

Another issue in the numerical discretization is to establish proper boundary conditions for handling the finite size of computational mesh. In this case, the boundary condition considered for the electrodes is the Dirichlet boundary condition, i.e., a perfect electric conductor (PEC) material is assumed and thus a fixed electrostatic potential $\phi = V_a + \phi_b$ where V_a and ϕ_b are the voltage source and built-in potential, respectively. Furthermore, a constant value of the carrier concentration in equilibrium is assumed for the metal–semiconductor junction in the electrodes

$$n|_{\text{elec}} = \frac{\sqrt{C^2 + 4n_i^2} + C}{2} \tag{20}$$

$$p|_{\text{elec}} = \frac{\sqrt{C^2 + 4n_i^2} - C}{2}. \tag{21}$$

For the interface vacuum-semiconductor, the following Neumann boundary condition is applied:

$$\varepsilon_r \left.\frac{\partial \phi}{\partial \hat{n}}\right|_{\text{sem}} = \left.\frac{\partial \phi}{\partial \hat{n}}\right|_{\text{vac}} \tag{22}$$

where $|_{\text{sem}}$ and $|_{\text{vac}}$ stand for normal derivative applied to points located at the boundary in the direction of the semiconductor and vacuum, respectively. For carrier distributions, the boundary conditions applied are:

$$\left.\frac{\partial n}{\partial \hat{n}}\right|_{\text{sem}} = 0 \tag{23}$$

$$\left.\frac{\partial p}{\partial \hat{n}}\right|_{\text{sem}} = 0. \tag{24}$$

Regarding the transient stage, discretization is based of the FDTD [35], which solves Maxwell's equations at discrete timesteps m, corresponding to $t = m\Delta t$, where Δt is the time interval of analysis. For semiconductors, the continuity equations will be considered by modifying the Yee's cell [36]. Fig. 2 shows the discrete unknowns on the new Yee's cell used in our simulator [17], [23].

Numerical formulation of FDTD is achieved by considering the transient current $\vec{J}_t(\vec{r}, t)$, which can be calculated by using (8), (9), and (4) to yield

$$\begin{aligned} \vec{J}_t(\vec{r}, t) &= \vec{J}(\vec{r}, t) - \vec{J}_0(\vec{r}) \\ &= \vec{J}_s(\vec{r}, t) + (\sigma_0(\vec{r}) + \sigma(\vec{r}, t))\, \vec{E}(\vec{r}, t) \end{aligned} \tag{25}$$

where

$$\begin{aligned} \vec{J}_s(\vec{r}, t) &= \sigma(\vec{r}, t)\, \vec{E}_0(\vec{r}) + qV_T\mu_n(\vec{r})\nabla n(\vec{r}, t) \\ &\quad - qV_T\mu_p(\vec{r})\nabla p(\vec{r}, t) \end{aligned} \tag{26}$$

$$\sigma_0(\vec{r}) = q\left(\mu_n(\vec{r})n0(\vec{r}) + \mu_p(\vec{r})p0(\vec{r})\right) \tag{27}$$

$$\sigma(\vec{r}, t) = q\left(\mu_n(\vec{r})n(\vec{r}, t) + \mu_p(\vec{r})p(\vec{r}, t)\right). \tag{28}$$

Source current at mth timestep $\vec{J}_s^m$ can be rewritten in terms of electrostatic field and time-dependent conductivity, $\vec{E}_0$ and σ^m, respectively, as

$$\vec{J}_s^m = \sigma^m \vec{E}_0 + qV_T\left(\mu_n \nabla n^m - \mu_p \nabla p^m\right). \tag{29}$$

Then, transient current is introduced in discrete form of Ampere's equation (7) as

$$\begin{aligned} \frac{\vec{E}^{m+1/2} - \vec{E}^{m-1/2}}{\varepsilon\Delta t} &= \nabla \wedge \vec{H}^m - \vec{J}_s^m \\ &\quad - (\sigma_0 + \sigma^m)\,\frac{\vec{E}^{m+1/2} + \vec{E}^{m-1/2}}{2} \end{aligned} \tag{30}$$

which enables a split formulation of Ampere-Maxwell and Faraday laws, of the form

$$\vec{E}^{m+1/2} = C_a^m \vec{E}^{m-1/2} + C_b^m \left(\nabla \wedge \vec{H}^m - \vec{J}_s^m\right) \tag{31}$$

$$\vec{H}^{m+1} = \vec{H}^m - \mu_0^{-1}\left(\nabla \wedge \vec{E}^{m+1/2}\right) \tag{32}$$

where

$$C_a^m = \frac{2\varepsilon - \Delta t(\sigma^m + \sigma_0)}{2\varepsilon + \Delta t(\sigma^m + \sigma_0)} \tag{33}$$

$$C_b^m = \frac{2\Delta t}{2\varepsilon + \Delta t(\sigma^m + \sigma_0)}. \tag{34}$$

A noteworthy numerical issue may arise if $C_a^m < 0$, requiring a modification of the auxiliary constants [37]

$$C_a^m = e^{-\Delta t(\sigma^m + \sigma_0)/\varepsilon} \tag{35}$$

$$C_b^m = \frac{1 - e^{-\Delta t(\sigma^m + \sigma_0)/\varepsilon}}{\sigma^m + \sigma_0}. \tag{36}$$

It also bears remarking that proposed procedure is prone to instabilities in the numerical solution. To avoid this, the Courant stability condition still holds for the solution of the combined drift-diffusion and FDTD scheme, but other challenging issues appear in this case which differ from the usual electromagnetic

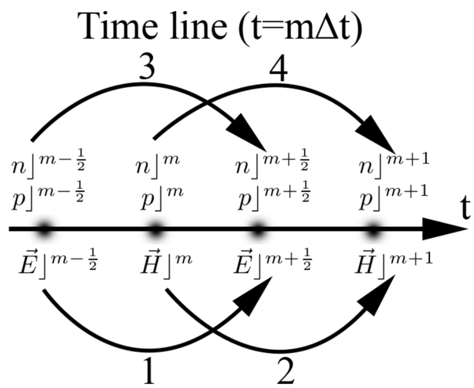

Fig. 3. Scheme of stable marching-on in-time procedure.

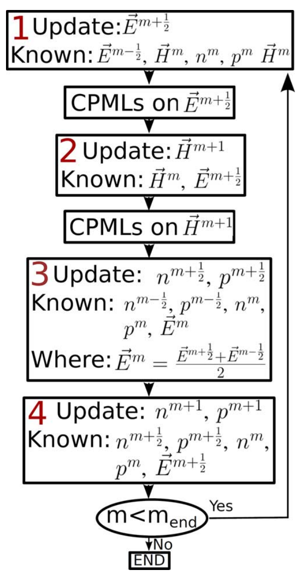

Fig. 4. Flowchart diagram of the transient stage. Numbers at the left part are related update procedure of Fig. 3.

case: on one hand, the complete system of equations is nonlinear, because of the recombination function (12) appearing in (10) and (11) and, on the other hand, terms related to distribution of carriers n^m and p^m act as diffusive sources of the electromagnetic field. Stable and accurate results are achieved by a double update of the distribution of carriers for each of the electromagnetic fields, as shown in Figs. 3 and 4.

Also, the marching-on-in-time procedure for carriers is updated by

$$n^{m+1/2} = n^{m-1/2} - \Delta t \left[RG^m + V_T^{-1} \sum_{w=1}^{3} \left(\bar{\beta}_{nw}^m \left(\bar{n}_w^m \right)^T \right) \right] \tag{37}$$

$$p^{m+1/2} = p^{m-1/2} - \Delta t \left[RG^m + V_T^{-1} \sum_{w=1}^{3} \left(\bar{\beta}_{pw}^m \left(\bar{p}_w^m \right)^T \right) \right] \tag{38}$$

as a solution in the $(m+1/2)$th time step, where the net recombination-generation rate is noted as $RG^m = R^m - G^m$. It is worth noting that, at the mth timestep, the electric field is

TABLE I
PARAMETERS USED IN THE SIMULATIONS

LT-GaAs: parameters used in the simulation (T=300k)	
Recombination function parameters	
Electrons	Holes
$\tau_n = 0.3ps$ [38]	$\tau_p = 0.4ps$ [38]
$C_{An} = 7 \cdot 10^{-30} cm^6 s^{-1}$ [39]	$C_{Ap} = 7 \cdot 10^{-30} cm^6 s^{-1}$ [39]
$n_1 = 4.5 \cdot 10^6 cm^{-3}$	$p_1 = 4.5 \cdot 10^6 cm^{-3}$
Doping and intrinsic concentration	
$N_D^+ = 1.3 \cdot 10^{16} cm^{-3}$	$n_i = 9 \cdot 10^6 cm^{-3}$ [40]
Mobility model [41] parameters	
$\mu_{n0} = 8000 \frac{cm^2}{Vs}$ [42]	$\mu_{p0} = 400 \frac{cm^2}{Vs}$ [42]
Relative permittivity and permeability	
$\varepsilon_r = 13.26$ if $\omega < 6THz$ [43]	$\mu_r = 1.0$
The laser and carriers generating rate function parameters	
$\alpha = 1.0 \mu m^{-1}$ [34]	T=(1-R)=0.9999
$\xi = 0.9999$	$\lambda_\gamma = 780nm$
$I_0 = 5 \frac{W}{\mu m^2}$	$\sigma_x = 1.8 \mu m$
$n_{GaAs}(\lambda_\gamma) = 3.83$ [44]	$\sigma_y = 1.8 \mu m$
$v_m = \frac{c_0}{n_{GaAs}}$	$\sigma_t = 80fs$
$P_{opt,av} = 0.63mW$	$\nu_\gamma = 80MHz$
Applied bias: 30V	

interpolated as $\vec{E}^m = (\vec{E}^{m+1/2} + \vec{E}^{m-1/2})/(2)$, while in the $(m+1)$th timestep this interpolation is no longer needed because the electric field $\vec{E}^{m+1/2}$ is known. Notably, in (37) and (38), it has been considered that $n^{-1/2} = p^{-1/2} = n^0 = p^0 = \vec{E}^{-1/2} = \vec{H}^0 = 0$, because steady-state distributions have been explicitly taking into account through the variables σ_0, $\vec{E}_0$ in the coefficients C_a^m, C_b^m, $\vec{J}_s^m$ of (31) and (32).

Regarding the boundary conditions of the FDTD method, the convolutional perfectly matched layers (CPMLs) are used [35]. Details of notation and the explicit discretized formulation are given in the Appendix A. For the sake of clarity, a complete flowchart diagram for the calculation is presented in Fig. 4.

IV. RESULTS

As will be shown, the procedures described above provide satisfactory results when compared with experimental measurements [10]. However, slight differences are detected, mostly due to the inherent complexity of a detailed numerical model of the laboratory setups. A high number of physical values, often omitted in reports of the experiments, are required to form a full computational model. Thus, some of them have been assumed to be typical values reported in the literature. A summary of the used values is presented in Table I, which lists the numerical values used for LT-GaAs, the source laser, and the bias electrodes. At this point, it should be noted that different values of the parameters can be found in previous papers, and Table I includes references from which they were extracted.

For validation purposes, the geometries of the electrodes implemented (Fig. 1) correspond to those described in [10] and [26]: the face-to-face (FF) dipole, where a small region with high electrostatic fields is created, and the strip-line (SL) dipole, where a large region of uniform electrostatic fields exists. Steady-state results are summarized in Fig. 5. The 3-D image of the electrostatic potential of Fig. 5(a) depicts the abrupt change in the inner region of the electrodes, where the

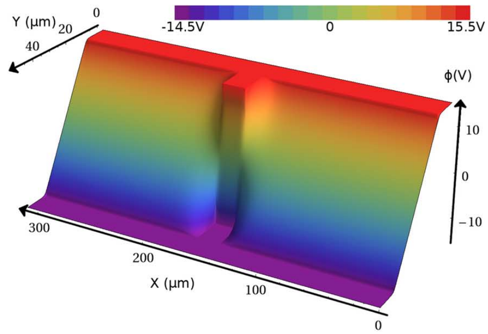

(a)

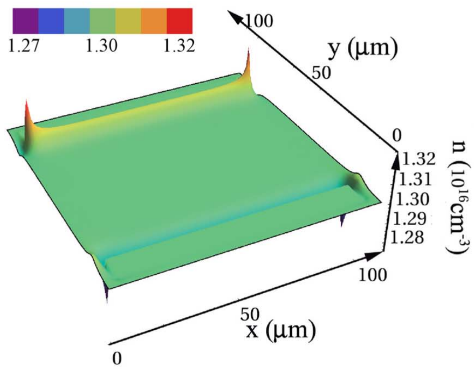

(b)

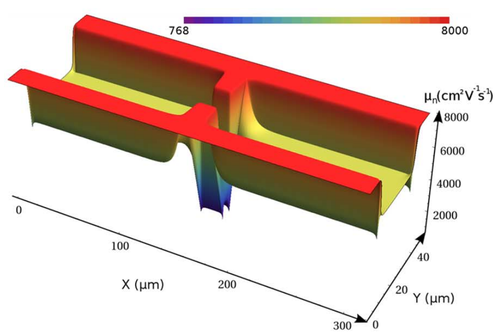

(c)

Fig. 5. Steady-state distribution of: (a) electrostatic potential for the FF dipole, (b) n-carriers for the SL dipole, and (c) mobility of n-carriers for the FF dipole.

source laser acts, and it has been validated using a specialized CAD for electronics [33], [29]. The high value of the subsequent electrostatic fields creates a significant drift for photogenerated carriers, thus starting the physical processes to generate THz radiation. Similar results are achieved for the SL dipole. In this case, Fig. 5(b) shows the distribution of n-charges. There is a noticeable accumulation of negative carriers around the electrodes, which needs to be taken into account because the source laser is usually applied near the electrodes in practical application using this PCA. Another noteworthy effect is the presence of strong nonlinear accumulations under the tips of the electrodes, which justifies the attention paid for an adequate computational model in this work. Fig. 5(c) illustrates the nonhomogeneous mobility of n-carriers for the FF dipole, calculated by applying at each point of the semiconductor a parallel-field model of the mobility. Thus, electrostatic field decreases substantially the μ_{n0} of Table I (meaning for the mobility of n-carriers in the absence of electric field).

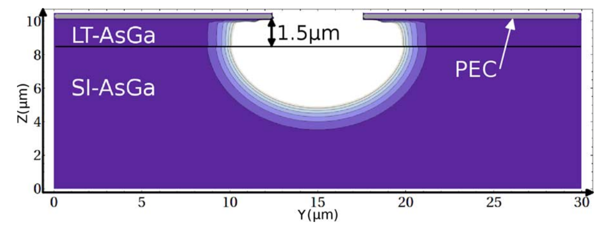

Fig. 6. Photogeneration of electric field at the semiconductor.

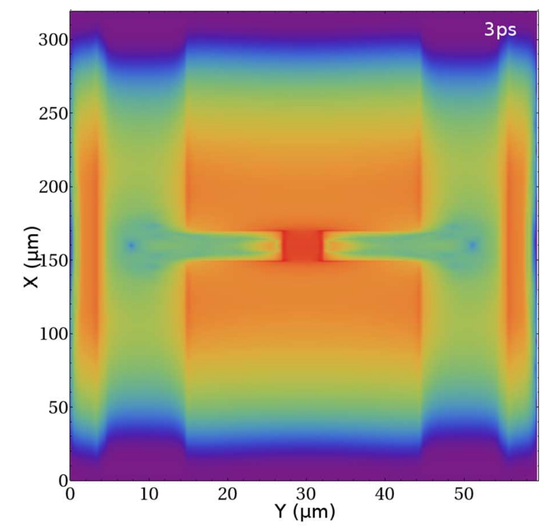

(a)

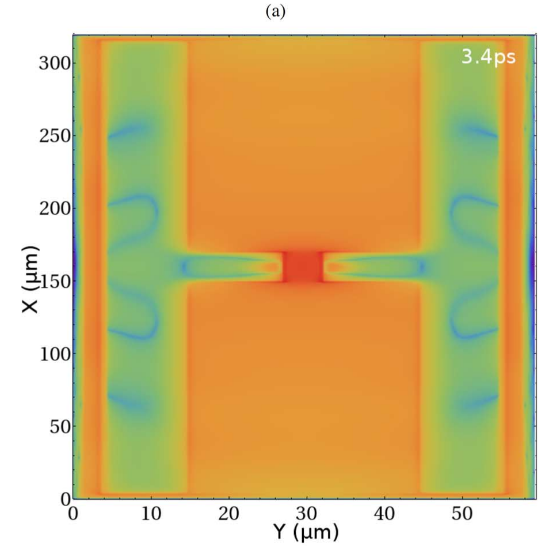

(b)

Fig. 7. Distribution of the transient current density at the interface of electrodes and LT- GaAs for the FF-dipole: (a) 3 ps and (b) 3.4 ps.

The transient stage begins with the incoming laser pulse. This generation phase is characterized for the generation of pairs (e-h) in the semiconductor. In practice, a thin layer of photosensitive LT-GaAs is placed on the top of a semi-insulating GaAs [45], thereby creating a transient electromagnetic field. Fig. 6 illustrates this, showing also that parallel electric-field predominates in LT-GaAs, justifying the use of parallel mobility models [32], as pointed out in Section II.

Fig. 7 illustrates the induced current pulse on the interface vacuum-semiconductor. Induced currents propagate in time

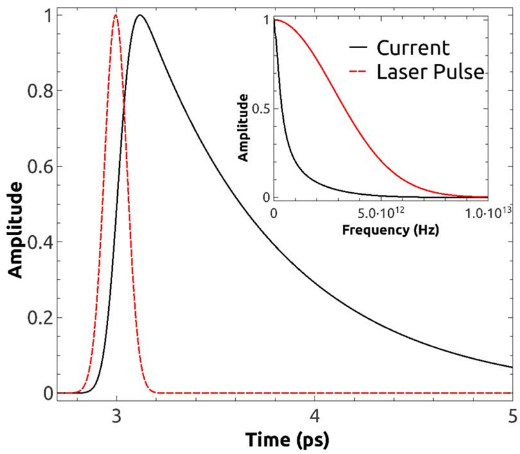

Fig. 8. Comparison of laser pulse and transient photogenerated current. For the sake of comparison, both lines were normalized to 3.14 A·μm^{-3} and 0.02 A·μm^{-2}, respectively.

along the geometry of electrodes, located at the left and right of the figure, in similar to the electric currents at RF and microwave dipole antennas. Then, the discontinuities of electrodes act as sources of radiating electromagnetic field [46], and they resonate at frequencies directly related to the length of the dipole [47].

Another remarkable fact is the influence of the recombination process in the bandwidth of the radiated field. Fig. 8 compares in the time and frequency domains the laser pulse and the photogenerated current at the center of the spot. It can be appreciated that the rise time of the induced current is influenced mainly by the waveform of the laser pulse, but, for the case of the decay time, the main factor to be considered is the recombination of photocarriers. Consequently, the bandwidth of the current decreases in comparison to the laser bandwidth, and the electromagnetic field is radiated in the THz regime.

Finally, the validation of the results is shown in the Fig. 9, where a good agreement between the computational predictions and the experimental data [10] is found for the radiated electromagnetic field in the broadside direction, for FF and SL dipoles. Differences arising for the time-domain responses are again justified by the complexity of the experimental setups. For considering the effect of the dielectric lens ($\mathrm{d} = 2.7$ cm), the semi-analytical approaches of [48] and [49] are applied to the radiated electromagnetic field, derived through a near-to-far-field FDTD algorithm [50]. Also, the receiving antenna effect is taken into account as proposed in [51], and the received current waveform is evaluated by applying

$$i_{\mathrm{rec}}(\tau) \propto \int \sigma_{rec}(t-\tau) E_{\mathrm{THz}}(t) dt \qquad (39)$$

where $E_{\mathrm{THz}}(t)$ corresponds to the radiated electromagnetic field calculated by the FDTD procedure, and $\sigma_{\mathrm{rec}}(t)$ is the photoconductance of the receiving PCA, which has been taken as the waveform of transient photogeneration depicted in Fig. 8.

At this point, it also bears remarking that similar results (i.e., radiated electromagnetic field) can be successfully reproduced

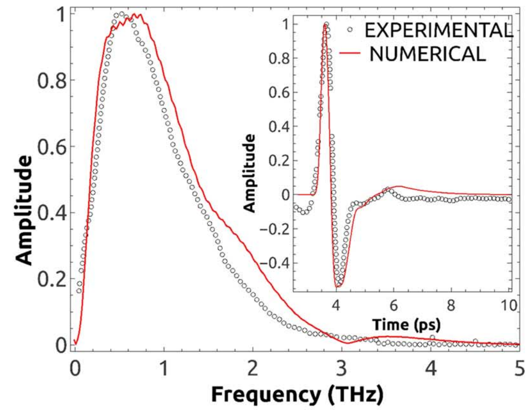

(a)

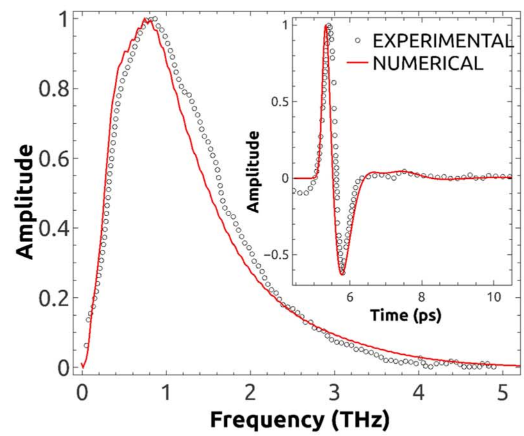

(b)

Fig. 9. Comparison of detected pulse from the radiated electromagnetic field rE_θ in the broadside direction ($\theta = 90°$, $\varphi = 0°$), showing experimental and numerical responses for the FF (upper) and SL (lower) dipoles. For sake of comparison, simulated responses of time-domain graphs were normalized to (a) 0.186 μA and (b) 56.6 nA.

by semi-analytical methods [15], [16], which are computationally faster than the presented procedure. As was stated in the Introduction, full-wave methods are useful for cases where simpler approaches are not applicable and for those aimed to provide a physical analysis of PCAs. On the other hand, a full-wave model of lenses is computationally demanding, and other approaches as asymptotic method-of-moments [52] can be also useful for the analysis and simulation of these devices.

V. Conclusion

Numerical simulations of PCAs can be implemented through a combined drift-diffusion and Maxwell equations model. For this purpose, the well-known FDTD procedure can be used. A key factor for achieving satisfactory results is to provide an adequate treatment of the steady model and time-update procedure, which is accomplished by applying nonlinear (Bernoulli) functions for the local distribution of carriers. Results not only validate of the code with experimental results but also demonstrate the potential of the method for analyzing the physical phenomena involved through the observation of the inner electromagnetic fields. In summary, the main contribution of this paper is the presentation of specific equations to THz researchers for their implementation as simulation tools in THz experiments.

APPENDIX
OPERATIONAL EQUATIONS FOR THE SIMULATION

For the sake of compactness, operational expressions arising from the discretization of the theoretical equations have been omitted in the main text. Here, the main results are presented in a matrix and ready-to-implement formulation. Also, it bears mentioning that the symbol $\odot$ is used to represent an element-by-element matrix product.

For a discrete spatial point $\{i, j, k\}$ of the mesh at a discrete time m, the discrete form of the carrier distribution surrounding that point in the x, y and z directions can be defined as

$$\widetilde{n}^m = \begin{pmatrix} \bar{n}_1^m \\ \bar{n}_2^m \\ \bar{n}_3^m \end{pmatrix} = \begin{pmatrix} n_{i+1,j,k}^m & n_{i,j,k}^m & n_{i-1,j,k}^m \\ n_{i,j+1,k}^m & n_{i,j,k}^m & n_{i,j-1,k}^m \\ n_{i,j,k+1}^m & n_{i,j,k}^m & n_{i,j,k-1}^m \end{pmatrix} \tag{40}$$

for the electrons. Similarly, for holes, this is

$$\widetilde{p}^m = \begin{pmatrix} \bar{p}_1^m \\ \bar{p}_2^m \\ \bar{p}_3^m \end{pmatrix} = \begin{pmatrix} p_{i+1,j,k}^m & p_{i,j,k}^m & p_{i-1,j,k}^m \\ p_{i,j+1,k}^m & p_{i,j,k}^m & p_{i,j-1,k}^m \\ p_{i,j,k+1}^m & p_{i,j,k}^m & p_{i,j,k-1}^m \end{pmatrix}. \tag{41}$$

The discrete potential matrix surrounding the considered point $\{i, j, k\}$ is

$$\widetilde{\phi} = \begin{pmatrix} \bar{\phi}_1 \\ \bar{\phi}_2 \end{pmatrix} = \begin{pmatrix} \phi_{i+1,j,k} & \phi_{i,j+1,k} & \phi_{i,j,k+1} \\ \phi_{i-1,j,k} & \phi_{i,j-1,k} & \phi_{i,j,k-1} \end{pmatrix}. \tag{42}$$

Also, a matrix of coefficients involving useful coefficients related to the step sizes Δx_i, Δy_j, and Δz_k of a nonuniform mesh is introduced as follows:

$$\widetilde{\delta} = \begin{pmatrix} \bar{\delta}_1 \\ \bar{\delta}_2 \end{pmatrix} = \begin{pmatrix} \delta_{11} & \delta_{12} & \delta_{13} \\ \delta_{21} & \delta_{22} & \delta_{23} \end{pmatrix} \tag{43}$$

where

$$\begin{aligned} \delta_{11} &= 2\left(\Delta x_i\left(\Delta x_i + \Delta x_{i-1}\right)\right)^{-1} \\ \delta_{12} &= 2\left(\Delta y_j\left(\Delta y_j + \Delta y_{j-1}\right)\right)^{-1} \\ \delta_{13} &= 2\left(\Delta z_k\left(\Delta z_k + \Delta z_{k-1}\right)\right)^{-1} \\ \delta_{21} &= 2\left(\Delta x_{i-1}\left(\Delta x_i + \Delta x_{i-1}\right)\right)^{-1} \\ \delta_{22} &= 2\left(\Delta y_{j-1}\left(\Delta y_j + \Delta y_{j-1}\right)\right)^{-1} \\ \delta_{22} &= 2\left(\Delta z_{k-1}\left(\Delta z_k + \Delta z_{k-1}\right)\right)^{-1} \end{aligned}$$

and the sum of spatial elements δ_Σ is also useful:

$$\delta_\Sigma = -\sum_{r=1}^{2}\sum_{w=1}^{3} \delta_{rw}.$$

Also, discrete mobilities for electrons and holes are reorganized as

$$\widetilde{\mu}_n = \begin{pmatrix} \bar{\mu}_{n_1} \\ \bar{\mu}_{n_2} \end{pmatrix} = \begin{pmatrix} \mu_n|_{i+1/2,j,k} & \mu_n|_{i,j+1/2,k} & \mu_n|_{i,j,k+1/2} \\ \mu_n|_{i-1/2,j,k} & \mu_n|_{i,j-1/2,k} & \mu_n|_{i,j,k-1/2} \end{pmatrix} \tag{44}$$

$$\widetilde{\mu}_p = \begin{pmatrix} \bar{\mu}_{p_1} \\ \bar{\mu}_{p_2} \end{pmatrix} = \begin{pmatrix} \mu_p|_{i+1/2,j,k} & \mu_p|_{i,j+1/2,k} & \mu_p|_{i,j,k+1/2} \\ \mu_p|_{i-1/2,j,k} & \mu_p|_{i,j-1/2,k} & \mu_p|_{i,j,k-1/2} \end{pmatrix} \tag{45}$$

and auxiliary matrices involving finite-difference coefficients and mobilities are then defined as

$$\widetilde{\mu}_n^* = \begin{pmatrix} \bar{\mu}_{n_1}^* \\ \bar{\mu}_{n_2}^* \end{pmatrix} = \widetilde{\delta} \odot \widetilde{\mu}_n = \begin{pmatrix} \delta_{11}\mu_{n_{11}} & \delta_{12}\mu_{n_{12}} & \delta_{13}\mu_{n_{13}} \\ \delta_{21}\mu_{n_{21}} & \delta_{22}\mu_{n_{22}} & \delta_{23}\mu_{n_{23}} \end{pmatrix} \tag{46}$$

$$\widetilde{\mu}_p^* = \begin{pmatrix} \bar{\mu}_{p_1}^* \\ \bar{\mu}_{p_2}^* \end{pmatrix} = \widetilde{\delta} \odot \widetilde{\mu}_p = \begin{pmatrix} \delta_{11}\mu_{p_{11}} & \delta_{12}\mu_{p_{12}} & \delta_{13}\mu_{p_{13}} \\ \delta_{21}\mu_{p_{21}} & \delta_{22}\mu_{p_{22}} & \delta_{23}\mu_{p_{23}} \end{pmatrix}. \tag{47}$$

Regarding the electric fields, a generalized form is assumed as follows:

$$\begin{aligned} \widetilde{E}^m &= \begin{pmatrix} \bar{E}_1^m \\ \bar{E}_2^m \end{pmatrix} \\ &= \begin{pmatrix} E_x|_{i+1/2,j,k}^m & E_y|_{i,j+1/2,k}^m & E_z|_{i,j,k+1/2}^m \\ E_x|_{i-1/2,j,k}^m & E_y|_{i,j-1/2,k}^m & E_z|_{i,j,k-1/2}^m \end{pmatrix}. \end{aligned} \tag{48}$$

The discrete form of the continuity (10) and (11) is written in terms of $(\widetilde{\beta}_n^m)$ and $(\widetilde{\beta}_p^m)$. To derive their operational expression, we define an auxiliary matrix

$$\widetilde{\wedge} = \begin{pmatrix} \bar{\wedge}_1 \\ \bar{\wedge}_2 \\ \bar{\wedge}_3 \\ \bar{\wedge}_4 \end{pmatrix} = V_T^{-1} \begin{pmatrix} -\Delta x_i & -\Delta y_j & -\Delta z_k \\ \Delta x_i & \Delta y_j & \Delta z_k \\ -\Delta x_{i-1} & -\Delta y_{j-1} & -\Delta z_{k-1} \\ \Delta x_{i-1} & \Delta y_{j-1} & \Delta z_{k-1} \end{pmatrix}. \tag{49}$$

Then, we introduce a combination of the modified mobilities and Bernoulli's functions

$$\widetilde{\varsigma}_n = \begin{pmatrix} \bar{\varsigma}_{n_1}^m \\ \bar{\varsigma}_{n_2}^m \\ \bar{\varsigma}_{n_3}^m \\ \bar{\varsigma}_{n_4}^m \end{pmatrix} = \begin{pmatrix} \bar{\mu}_{n_1}^* \odot B\left(\bar{\wedge}_1 \odot \bar{E}_1^m\right) \\ \bar{\mu}_{n_1}^* \odot B\left(\bar{\wedge}_2 \odot \bar{E}_1^m\right) \\ \bar{\mu}_{n_2}^* \odot B\left(\bar{\wedge}_3 \odot \bar{E}_2^m\right) \\ \bar{\mu}_{n_2}^* \odot B\left(\bar{\wedge}_4 \odot \bar{E}_2^m\right) \end{pmatrix} \tag{50}$$

and

$$\widetilde{\varsigma}_p = \begin{pmatrix} \bar{\varsigma}_{p_1}^m \\ \bar{\varsigma}_{p_2}^m \\ \bar{\varsigma}_{p_3}^m \\ \bar{\varsigma}_{p_4}^m \end{pmatrix} = \begin{pmatrix} \bar{\mu}_{p_1}^* \odot B\left(\bar{\wedge}_1 \odot \bar{E}_1^m\right) \\ \bar{\mu}_{p_1}^* \odot B\left(\bar{\wedge}_2 \odot \bar{E}_1^m\right) \\ \bar{\mu}_{p_2}^* \odot B\left(\bar{\wedge}_3 \odot \bar{E}_2^m\right) \\ \bar{\mu}_{p_2}^* \odot B\left(\bar{\wedge}_4 \odot \bar{E}_2^m\right) \end{pmatrix} \tag{51}$$

which allows the calculation of auxiliary matrices $\widetilde{\beta}_n^m$ and $\widetilde{\beta}_p^m$ of the form

$$\widetilde{\beta}_n^m = \begin{pmatrix} \bar{\beta}_{n_1}^m \\ \bar{\beta}_{n_2}^m \\ \bar{\beta}_{n_3}^m \end{pmatrix} = \begin{pmatrix} \bar{\varsigma}_{n_1}^m \\ -\bar{\varsigma}_{n_2}^m - \bar{\varsigma}_{n_3}^m \\ \bar{\varsigma}_{n_4}^m \end{pmatrix} \tag{52}$$

and

$$\widetilde{\beta}_p^m = \begin{pmatrix} \bar{\beta}_{p_1}^m \\ \bar{\beta}_{p_2}^m \\ \bar{\beta}_{p_3}^m \end{pmatrix} = \begin{pmatrix} \bar{\varsigma}_{p_3}^m \\ -\bar{\varsigma}_{p_1}^m - \bar{\varsigma}_{p_4}^m \\ \bar{\varsigma}_{p_2}^m \end{pmatrix}. \tag{53}$$

For the steady-state solution, the dependence of (31) is expressed in terms of the scalar electric potential ϕ of the form

$$\widetilde{E}_0 = \begin{pmatrix} \frac{\phi_{i,j,k}-\phi_{i+1,j,k}}{\Delta x_i} & \frac{\phi_{i,j,k}-\phi_{i,j+1,k}}{\Delta y_j} & \frac{\phi_{i,j,k}-\phi_{i,j,k+1}}{\Delta z_k} \\ \frac{\phi_{i-1,j,k}-\phi_{i,j,k}}{\Delta x_{i-1}} & \frac{\phi_{i,j-1,k}-\phi_{i,j,k}}{\Delta y_{j-1}} & \frac{\phi_{i,j,k-1}-\phi_{i,j,k}}{\Delta z_{k-1}} \end{pmatrix} = \begin{pmatrix} \bar{E}_{0,1} \\ \bar{E}_{0,2} \end{pmatrix} \tag{54}$$

and steady-state distribution of carriers is

$$\widetilde{n0} = \begin{pmatrix} \bar{n0}_1 \\ \bar{n0}_2 \\ \bar{n0}_3 \end{pmatrix} = \begin{pmatrix} n0_{i+1,j,k} & n0_{i,j,k} & n0_{i-1,j,k} \\ n0_{i,j+1,k} & n0_{i,j,k} & n0_{i,j-1,k} \\ n0_{i,j,k+1} & n0_{i,j,k} & n0_{i,j,k-1} \end{pmatrix} \tag{55}$$

for the electrons. Also

$$\widetilde{p0} = \begin{pmatrix} \bar{p0}_1 \\ \bar{p0}_2 \\ \bar{p0}_3 \end{pmatrix} = \begin{pmatrix} p0_{i+1,j,k} & p0_{i,j,k} & p0_{i-1,j,k} \\ p0_{i,j+1,k} & p0_{i,j,k} & p0_{i,j-1,k} \\ p0_{i,j,k+1} & p0_{i,j,k} & p0_{i,j,k-1} \end{pmatrix} \tag{56}$$

for holes. Auxiliary matrices $\widetilde{\beta}_{n0}$ and $\widetilde{\beta}_{p0}$ are defined equivalently to (52) and (53) in the form

$$\widetilde{\beta}_{n0} = \begin{pmatrix} \bar{\beta}_{n0_1} \\ \bar{\beta}_{n0_2} \\ \bar{\beta}_{n0_3} \end{pmatrix} = \begin{pmatrix} \bar{\varsigma}_{n0_1} \\ -\bar{\varsigma}_{n0_2} - \bar{\varsigma}_{n0_3} \\ \bar{\varsigma}_{n0_4} \end{pmatrix} \tag{57}$$

and

$$\widetilde{\beta}_{p0} = \begin{pmatrix} \bar{\beta}_{p0_1} \\ \bar{\beta}_{p0_2} \\ \bar{\beta}_{p0_3} \end{pmatrix} = \begin{pmatrix} \bar{\varsigma}_{p0_3} \\ -\bar{\varsigma}_{p0_1} - \bar{\varsigma}_{p0_4} \\ \bar{\varsigma}_{p0_2} \end{pmatrix} \tag{58}$$

where

$$\begin{pmatrix} \bar{\varsigma}_{n0_1} \\ \bar{\varsigma}_{n0_2} \\ \bar{\varsigma}_{n0_3} \\ \bar{\varsigma}_{n0_4} \end{pmatrix} = \begin{pmatrix} \bar{\mu}^*_{n_1} \odot B\left(\bar{\Lambda}_1 \odot \bar{E}_{0,1}\right) \\ \bar{\mu}^*_{n_1} \odot B\left(\bar{\Lambda}_2 \odot \bar{E}_{0,1}\right) \\ \bar{\mu}^*_{n_2} \odot B\left(\bar{\Lambda}_3 \odot \bar{E}_{0,2}\right) \\ \bar{\mu}^*_{n_2} \odot B\left(\bar{\Lambda}_4 \odot \bar{E}_{0,2}\right) \end{pmatrix} \tag{59}$$

and

$$\begin{pmatrix} \bar{\varsigma}_{p0_1} \\ \bar{\varsigma}_{p0_2} \\ \bar{\varsigma}_{p0_3} \\ \bar{\varsigma}_{p0_4} \end{pmatrix} = \begin{pmatrix} \bar{\mu}^*_{p_1} \odot B\left(\bar{\Lambda}_1 \odot \bar{E}_{0,1}\right) \\ \bar{\mu}^*_{p_1} \odot B\left(\bar{\Lambda}_2 \odot \bar{E}_{0,1}\right) \\ \bar{\mu}^*_{p_2} \odot B\left(\bar{\Lambda}_3 \odot \bar{E}_{0,2}\right) \\ \bar{\mu}^*_{p_2} \odot B\left(\bar{\Lambda}_4 \odot \bar{E}_{0,2}\right) \end{pmatrix}. \tag{60}$$

REFERENCES

[1] G. Chattopadhyay, "Technology, capabilities, and performance of low power terahertz sources," *IEEE Trans. THz Sci. Technol.*, vol. 1, no. 1, pp. 33–53, Sep. 2011.

[2] M. S. Vitiello and A. Tredicucci, "Tunable emission in THz quantum cascade lasers," *IEEE Trans. THz Sci. Technol.*, vol. 1, no. 1, pp. 76–84, Sep. 2011.

[3] J. H. Booske, R. J. Dobbs, C. D. Joye, C. L. Kory, G. R. Neil, G. S. Park, J. Park, and R. J. Temkin, "Vacuum electronic high power terahertz sources," *IEEE Trans. THz Sci. Technol.*, vol. 1, no. 1, pp. 54–75, Sep. 2011.

[4] H.-J. Song and T. Nagatsuma, "Present and future of terahertz communications," *IEEE Trans. THz Sci. Technol.*, vol. 1, no. 1, pp. 256–263, Sep. 2011.

[5] D. Grischkowsky, N. Katzenellenbogen, and H. Harde, "Time-domain spectroscopy with femtosecond pulses of THz radiation," *Nonlinear Opt.: Mater., Fundam., Applicant. Tech. Dig.*, vol. 18, pp. 187–188, 1992.

[6] N. Khiabani, Y. Huang, Y. Shen, and S. Boyes, "Theoretical modeling of a photoconductive antenna in a terahertz pulsed system," *IEEE Trans. Antennas Propag.*, vol. 61, no. 4, pp. 1538–1546, Apr. 2013.

[7] D. Auston and M. Nuss, "Electrooptical generation and detection of femtosecond electrical transients," *IEEE J. Quantum Electron.*, vol. 24, no. 2, pp. 184–197, Feb. 1988.

[8] G. Morou, C. V. Stancampiano, A. Antonetti, and A. Orszag, "Picosecond microwave pulses generated with a subpicosecond laser-driven semiconductor switch," *Appl Phys Lett*, vol. 39, no. 4, pp. 295–296, 1981.

[9] J. T. Darrow, X. C. Zhang, D. H. Auston, and J. D. Morse, "Saturation properties of large-aperture photoconducting antennas," *IEEE J. Quantum Electron.*, vol. 28, no. 6, pp. 1607–1616, Jun. 1992.

[10] M. Tani, S. Matsuura, K. Sakai, and S. I. Nakashima, "Emission characteristics of photoconductive antennas based on low-temperature-grown GaAs and semi-insulating GaAs," *J. Opt. Soc. Amer.*, vol. 36, pp. 7853–7859, 1997.

[11] L. Hou and W. Shi, "An LT-GaAs terahertz photoconductive antenna with high emission power, low noise, and good stability," *IEEE Trans. Electron Devices*, vol. 60, no. 5, pp. 1619–1624, May 2013.

[12] S. Masato and T. Masayoshi, "Fe-implanted InGaAs photoconductive terahertz detectors triggered by 1.55 μm femtosecond optical pulses," *Appl Phys Lett*, vol. 86, no. 16, 2005, Art. ID 163504.

[13] I. Kostakis, D. Saeedkia, and M. Missous, "Terahertz generation and detection using low temperature grown InGaAs-InAlAs photoconductive antennas at 1.55 μm pulse excitation," *IEEE Trans. THz Sci. Technol.*, vol. 2, no. 6, pp. 617–622, Nov. 2012.

[14] J. H. Strait, P. A. George, J. Dawlaty, S. Shivaraman, M. Chandrashekhar, F. Rana, and M. G. Spencer, "Emission of terahertz radiation from SiC," *Appl Phys Lett*, vol. 95, no. 5, 2005, Art. ID 051912.

[15] S.-G. Park, A. Weiner, M. Melloch, C. Sider, J. Sider, and A. J. Taylor, "High-power narrow-band terahertz generation using large-aperture photoconductors," *IEEE J. Quantum Electron.*, vol. 35, no. 8, pp. 1257–1268, Aug. 1999.

[16] L. Duvillaret, F. Garet, J.-F. Roux, and J.-L. Coutaz, "Analytical modeling and optimization of terahertz time-domain spectroscopy experiments, using photoswitches as antennas," *IEEE J. Sel. Topics Quantum Electron.*, vol. 7, no. 4, pp. 615–623, Jul.–Aug. 2001.

[17] E. Sano and T. Shibata, "Fullwave analysis of picosecond photoconductive switches," *IEEE J. Quantum Electron.*, vol. 26, no. 3, pp. 372–377, Mar. 1990.

[18] J. Zhang, Z. Chen, and X. Chen, "FDTD analysis of photoconducting antennas for millimeter-wave generation," *Int. J. RF Microw. Comput.-Aided Eng.*, vol. 10, no. 4, 2000, Art. ID 21322.

[19] A. Reineix, M. Ariaudo, C. Chatenet, and B. Jecko, "Theoretical analysis of photoconducting dipole antennas," *Microw. Opt. Technol. Lett.*, vol. 15, pp. 110–113, 1997.

[20] Z. Piao, M. Tani, and K. Sakai, "Carrier dynamics and terahertz radiation in photoconductive antennas," *Jpn. J. Appl. Phys.*, vol. 39, p. 96, 2000.

[21] S. Hughes, M. Tani, and K. Sakai, "Vector analysis of terahertz transients generated by photoconductive antennas in near- and far-field regimes," *J. Appl. Phys.*, vol. 93, pp. 4880–4884, 2003.

[22] R. Mirzavand, A. Abdipour, G. Moradi, and M. Movahhedi, "Full-wave semiconductor devices simulation using ADI-FDTD method," *Progr. Electromagn. Res. M*, vol. 11, pp. 191–202, 2010.

[23] P. Kirawanich, S. J. Yakura, and N. E. Islam, "Study of high-power wideband terahertz-pulse generation using integrated high-speed photoconductive semiconductor switches," *IEEE Trans. Plasma Sci.,* , vol. 37, no. 1, pp. 219–228, Jan. 2009.

[24] S. Selberherr, *Analysis and Semiconductor Devices*. Berlin, Germany: Springer-Verlag, 1984.

[25] M. Khabiri, M. Neshat, and S. Safavi-Naeini, "Hybrid computational simulation and study of continuous wave terahertz photomixers," *IEEE Trans. THz Sci. Technol.*, vol. 2, no. 6, pp. 605–616, Nov. 2012.

[26] Y. Cai, I. Brener, J. Lopata, J. Wynn, L. Pfeiffer, and J. Federici, "Design and performance of singular electric field terahertz photoconducting antennas," *Appl. Phys. Lett.*, vol. 71, pp. 2076–2078, 1997.

[27] J. D. Jackson and R. F. Fox, "Classical electrodynamics," *Amer. J. Phys.*, vol. 67, p. 841, 1999.
[28] E. Moreno, M. Pantoja, S. Garcia, J. Roldan, F. Ruiz, A. Bretones, and R. Martin, "On the simulation of carrier dynamics in terahertz photoconductive antennas," in *Proc. 7th Eur. Conf. IEEE Antennas Propag.*, 2013, pp. 749–750.
[29] E. Moreno-Perez, M. Pantoja, S. Garcia, A. R. Bretones, and R. G. Martín, "Time domain simulation of THz photoconductive antennas," in *Proc. 6th Eur. Conf. IEEE Antennas Propag.*, 2012, pp. 1054–1057.
[30] W. Shockley and W. T. Read, "Statistics of the recombinations of holes and electrons," *Phys. Rev.*, vol. 87, pp. 835–842, Sep. 1952.
[31] N. W. Ashcroft and N. D. Mermin, *Solid State Physics*, D. G. Crane, Ed. Orlando, FL, USA: H. C. Publishers, 1976.
[32] R. Caughey and D. M. Thomas, "Carrier mobilities in silicon empirically related to doping and field," *Proc. IEEE*, vol. 55, no. 12, pp. 2192–2193, Dec. 1967.
[33] *"ATLAS User's Manual: Device Simulation Software,"* SILVACO Int., 2010.
[34] B. E. S. M.C. Teich, *Fundamental of Photonics in Pure and Applied Optics*. Hoboken, NJ, USA: Wiley, 2007.
[35] A. Taflove and S. C. Hagness, *Computational Electrodynamics: The Finite-Differences Time Domain Method*. Boston, MA, USA: Artech House, 2005.
[36] K. Yee, D. Ingham, and K. Shlager, "Time-domain extrapolation to the far field based on FDTD calculations," *IEEE Trans. Antennas Propag.*, vol. 39, no. 3, pp. 410–413, Mar. 1991.
[37] P. Petropoulos, "Analysis of exponential time-differencing for FDTD in lossy dielectrics," *IEEE Trans. Antennas Propag.*, vol. 45, no. 6, pp. 1054–1057, Jun. 1997.
[38] D. C. Look, "Molecular beam epitaxial GaAs grown at low temperatures," *Thin Solid Films*, vol. 231, no. 1-2, pp. 61–73, 1993.
[39] U. Strauss, W. W. Ruhle, and K. Kohler, "Auger recombination in intrinsic GaAs," *Appl. Phys. Lett.*, vol. 62, no. 1, pp. 55–57, Jan. 1993.
[40] M. C. Richard, S. Muller, and T. I. Kamins, *Device Electronics for Integrated Circuits*, 3rd ed. New York, NY, USA: Wiley, 2002.
[41] *"VMC 2.0 User's Guide,"* Institut für Mikroelektronik, Technische Universität Wien, 2006.
[42] M. Kalusmeier-Brown, M. Lundstrom, and M. Melloch, "The effects of heavy impurity doping on AlGaAs/GaAs bipolar transistors," *IEEE Trans. Electron Devices*, vol. 10, no. 36, pp. 2146–2155, Oct. 1989.
[43] M. M. Sigalas, C. M. Soukoulis, C. T. Chan, and K. M. Ho, "Electromagnetic-wave propagation through dispersive and absorptive photonic-band-gap materials," *Phys. Rev. B*, vol. 49, no. 16, pp. 11080–11087, Apr. 1994.
[44] Filmetrics [Online]. Available: http://www.filmetrics.com/refractive-indexdatabase/GaAs/gallium-arsenide
[45] M. C. Beard, G. M. Turner, and C. A. Schmuttenmaer, "Subpicosecond carrier dynamics in low-temperature grown GaAs as measured by time-resolved terahertz spectroscopy," *J. Appl. Phys.*, vol. 90, no. 12, pp. 5915–5923, 2001.
[46] E. K. Miller, "Direct time-domain techniques for transient radiation and scattering from wires," *Proc. IEEE*, vol. 68, no. 11, pp. 1396–1423, Nov. 1980.
[47] Y.-S Lee, *Principles of Terahertz Science and Technology*, 1st ed. Berlin, Germany: Springer, 2009.
[48] P. U. Jepsen, R. Jacobsen, and S. Keiding, "Generation and detection of terahertz pulses from biased semiconductor antennas," *J. Opt. Soc. Amer. B*, vol. 13, no. 11, pp. 2424–2436, 1996.
[49] K. Ezdi, B. Heinen, C. Jördens, N. Vieweg, N. Krumbholz, R. Wilk, M. Mikulics, and M. Koch, "A hybrid time-domain model for pulsed terahertz dipole antennas," *J. Eur. Opt. Soc.*, vol. 4, pp. 09001-1–09001-7, 2009.
[50] S. G. Garcia, B. G. Olmedo, and R. G. Martin, "Time-domain near-to far-field transformation for FDTD in two dimensions," *Microw. Opt. Technol. Lett.*, vol. 27, no. 6, pp. 427–432, 2000.
[51] M. Tani, Y. Hirota, C. Que, S. Tanaka, R. Hattori, M. Yamaguchi, S. Nishizawa, and M. Hangyo, "Novel terahertz photoconductive antennas," *Int. J. Infrared Millimeter Waves*, vol. 27, pp. 531–546, 2006.
[52] N. Llombart and A. Neto, "THz time-domain sensing: The antenna dispersion problem and a possible solution," *IEEE Trans. THz Sci. Technol.*, , vol. 2, no. 4, pp. 416–423, Jul. 2012.

Enrique Moreno received the B.S. degree in applied physics and instrumentation from Cork Institute of Technology, Cork, Ireland, in 2008, and the M.S. degrees in fundamental physics and in advanced methods and techniques in physics in 2009 and 2010, respectively, from the University of Granada, Granada, Spain, where he is currently working toward the Ph.D. degree in physics in the Group of Electromagnetics of Granada.

Mario Fernández Pantoja (M'00–SM'12) received the B.Sc., M.Sc., and Ph.D. degrees in electrical engineering from the University of Granada, Granada, Spain, in 1996, 1998, and 2001, respectively.

Between 1997 to 2001, he was an Assistant Professor with the University of Jaen, Jaen, Spain. In 2001, he joined the University of Granada, Granada, Spain, where, in 2004, he was appointed Associate Professor and qualified as a Full Professor in 2012. He has been a Guest Researcher with the Dipartimento Ingenieria dell'Informazione, University of Pisa, Italy, the Antenna and Electromagnetics Group, Denmark Technical University, and Computational Electromagnetics and Antenna Research Laboratory from Pennsylvania State University. His research is mainly focused on the areas of interaction of electromagnetic waves with structures in time domain, optimization methods applied to antenna design, advanced computational methods and nanoelectromagnetics.

Salvador G. Garcia (M'03) was born in 1966 in Baeza, Spain. He received the M.S. and Ph.D. degrees (with extraordinary award) in physics from the University of Granada, Granada, Spain, in 1989 and 1994, respectively.

In 1999, he joined the Department of Electromagnetism and Matter Physics, University of Granada, Granada, Spain, as an Assistant Professor and qualified as a Full Professor in 2012. He has authored and coauthored over 50 refereed journal articles and book chapters and over 80 conference papers and technical reports, and he has participated in several national and international projects with public and private funding. He has received grants to stay as a Visiting Scholar at the University of Duisburg (1997), the Institute of Mobile and Satellite Communication Techniques (1998), the University of Wisconsin-Madison (2001), and the University of Kentucky (2005). His current research interests include computational electromagnetics, electromagnetic compatibility, terahertz technologies, microwave imaging and sensing (GPR), bioelectromagnetics, and antenna design.

Amelia Rubio Bretones (SM'99) received the Ph.D. degree in physics (*cum laude*) from the University of Granada, Granada, Spain, in 1988.

Since 1985 she has been with the Department of Electromagnetism, University of Granada, Granada, Spain, first as an Assistant Professor, an Associate Professor, and, since 2000, as a Full Professor. On several occasions, she was a Visiting Scientist with the Delft and Eindhoven Universities of Technologies (both in The Netherlands) and at the Pennsylvania State University. Her research expertise lies mainly in the field of numerical techniques for applied electromagnetics with an emphasis on time domain techniques such as finite difference time domain, the method of moments in the time domain with application in antenna and scattering problems, and GPR.

Dr. Bretones was co-chair of the 5th International Workshop on Advanced Ground Penetrating Radar, IWAGPR2009, held in Granada (Spain). She was the recipient of a Summa Foundation fellowship in 1997 and also of the International Union of Radio Science (URSI) Young Scientist Award in 1993 and 1995.

Rafael Gómez Martín (SM'00) received the M.Sc. degree from the University of Seville, Seville, Spain, in 1971, and the Ph.D. degree (*cum laude*) from the University of Granada, Granada, Spain, in 1974, both in physics.

Between 1971 and 1974, he was with the University of Santiago de Compostela, Spain, as a Ph.D. student. Between 1975 and 1985, he was an Associate Professor with the University of Granada, Granada, Spain, where in 1986 he became a Professor and is currently with the Department of Applied Physics. His current research interests include the development of analytical and numerical methods in electromagnetism, communication system design (wave guides, fiber optics, antennas and radar), electromagnetic compatibility, and biological effects of electromagnetic fields.